Engineering Analysis with Boundary Elements 150 (2023) 7–19

Contents lists available at ScienceDirect

Engineering Analysis with Boundary Elements

journal homepage: www.elsevier.com/locate/enganabound

Dual interpolation boundary face method for 3-D acoustic problems based on binary tree grids

Rongxiong Xiao [a], Jianming Zhang [a,*], Pengfei Chai [a], Chuanming Ju [b], WeiCheng Lin [a], Rui He [a]

[a] State Key Laboratory of Advanced Design and Manufacturing for Vehicle Body, College of Mechanical and Vehicle Engineering, Hunan University, Changsha 410082, China
[b] School of Engineering and Materials Science, Yantai University, Yantai 264005, China

ARTICLE INFO

Keywords:
DiBFM
Discontinuous grids
Meshless method
Burton-miller formulation

ABSTRACT

A dual interpolation boundary face method (DiBFM) based on binary tree grids is presented to solve 3-D acoustic problems in this paper. The boundary element method (BEM) is widely used to solve acoustic problems for its advantage of only discretizing boundaries and satisfying Sommerfeld radiation condition. Combining boundary integral equations with computer graphics, the boundary face method (BFM) is the enrichment of the BEM and is able to avoid the geometric errors between CAD and CAE models. By adding virtual nodes on the vertices and edges of tradition discontinuous elements, the dual interpolation elements are introduced and have higher interpolation accuracy. What's more, since there is no need for grids continuity, the binary tree grids can be applied to the implementation of the DiBFM, and have the ability to make mesh generation more automatic and easier. The Burton-Miller formulation is employed to remove the non-uniqueness issue. Several numerical examples are given to demonstrate the practicability and superiority of the proposed method.

1. Introduction

The boundary element method (BEM) as a numerical method has developed rapidly in recent decades. Since it has attractive characteristics of dimensionality reduction and high accuracy, the BEM has been used to various fields such as elasticity problems [1], contact problems [2], potential problems [3], acoustic problems [4]. Especially, the Sommerfeld radiation condition can be satisfied automatically at infinity in the boundary integral equation (BIE), thus the BEM is more suitable to handle infinite domain problems than the finite element method (FEM).

However, when applying the BEM based on the conventional boundary integral equation (CBIE) to solve the exterior Helmholtz equation, there will be non-uniqueness of solutions at certain frequencies [5]. This is a purely mathematical problem without any actual physical meaning. Two main approaches have been proposed to overcome this phenomenon, one is the combined Helmholtz integral equation formulation (CHIEF) [6] which adds internal integral points and then uses the least square method to solve the overdetermined equations. When dealing with complex structures or high-frequency problems, the CHIEF is not applicable because it is difficult to select the number and location of configuration points. The other more popular remedy to this problem is the Burton-Miller method [7]. Coupling the hypersingular boundary integral equation (HBIE) obtained by taking the normal derivative of the CBIE with the CBIE, the Burton-Miller formulation can yield unique solutions at all frequencies, and the hypersingular integrals are also introduced at the same time. The accurate calculation of singular integrals has always been a hotspot and difficulty in the study of the BEM, and there are also many mature processing methods, for instance, local coordinate approximate expansion [8], regularization [9], radial integration [10].

In addition, whether in the BEM or the FEM, the CAD and the CAE model are often independent of each other which will cause geometric errors. The boundary face method (BFM) [11–12] uses the boundary representation data of CAD solid modeling, the interpolation of integration and physical variables are both performed in the parameter space of the surface, CAE model agrees with CAD model. The dual interpolation element includes the source points located inside the element and the virtual points placed on the vertices and edges of the element. The advantage of the dual interpolation elements is that they can achieve high accuracy without increasing the calculation scale, and can unify the conforming and nonconforming elements. The DiBFM [13–14] is introduced by applying the dual interpolation element to the BFM. Two layer interpolations are implemented in the DiBFM. The

* Corresponding author at: College of Mechanical and Vehicle Engineering, Hunan University, Changsha 410082, China.
E-mail address: zhangjm@hnu.edu.cn (J. Zhang).

https://doi.org/10.1016/j.enganabound.2023.01.025
Received 27 August 2022; Received in revised form 1 January 2023; Accepted 25 January 2023
Available online 5 February 2023

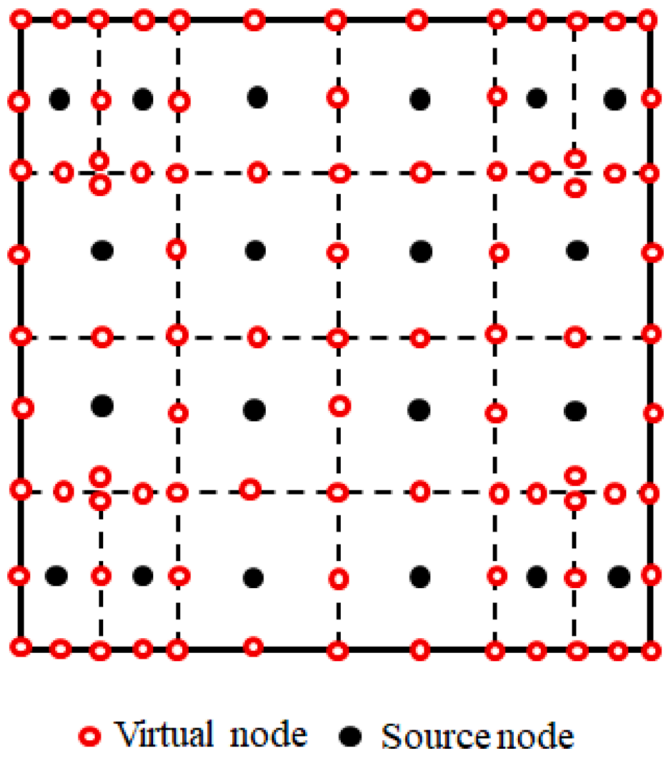

Fig. 1. The node layout of dual interpolation element.

first-layer interpolation is to use the Lagrange polynomials to approximate the physical quantities. The other is to condense the degree of freedom of virtual points. Moreover, the DiBFM makes full use of the property that the trail function of BIE does not need to be continuous, the boundaries can be discretized with the discontinuous grids. However, the main mesh generation algorithms of surface, such as, the Delaunay triangulation, advancing front method (AFM), only can generate continuous grids. The binary tree grids obtained by the binary tree subdivision method [15] include continuous and discontinuous grids, which greatly alleviates the task of mesh generation.

In this paper, the Hermite-type moving-least-squares (HMLS) approximation [16–17] is used as the second-layer interpolation in the DiBFM. Unlike the moving-least-squares (MLS) approximation [18], in the HMLS interpolation, the shape functions are directly established on the Cartesian coordinates without the parametric coordinates of the curve, and the influence domain can include multiple surfaces.

Section 2 introduces the dual interpolation method using binary tree grids. The DiBFM for 3-D acoustic problem is demonstrated in Section 3. Numerical examples are given in Section 4. Section 5 drafts the conclusions.

2. Dual interpolation method using binary tree grids

Based on the dual interpolation elements, the element interpolation and meshless function approximation are applied to the implementation of the dual interpolation method. As shown in Fig. 1, the dual interpolation elements include source and virtual nodes.

Taking a flange as an example, its binary tree grids are presented in Fig. 2. Since the discontinue grids are introduced, the grid density control is more flexible and free, and the size difference between adjacent grids can be twice. For the mesh generation algorithm, please refer to [15].

2.1. First-layer interpolation

Lagrange polynomials are used in this interpolation. The contributions of all nodes in a dual interpolation element are taken into account. For acoustic problems, the boundary variables are the sound pressure ϕ and sound flux$q$, and the forms of the first-layer interpolation are given as below:

$$\phi(\xi,\eta)=\sum_{i=1}^{n_i}N_i^s(\xi,\eta)\phi(Q_i^s)+\sum_{j=1}^{n_j}N_j^v(\xi,\eta)\phi\left(Q_j^v\right), \tag{1}$$

$$q(\xi,\eta)=\sum_{i=1}^{n_i}N_i^s(\xi,\eta)q(Q_i^s)+\sum_{j=1}^{n_j}N_j^v(\xi,\eta)q\left(Q_j^v\right), \tag{2}$$

where ξ and η represent the parameter space coordinates, n_i and n_j denote the number of source and virtual nodes, respectively. $\phi(Q_i)$, $q(Q_i)$, and $N_i(\xi,\eta)$ are the sound pressure, sound flux, and shape function, respectively.

2.2. Second-layer interpolation

To build the relationship between source and virtual nodes as shown in Fig. 3, the meshless method with HMLS approximation is introduced in this interpolation, and its forms are given below [14]:

$$\phi\left(Q_j^v\right)=\sum_{K=1}^{L}\phi_K^{uu}(x^v,y^v,z^v)\widehat{\phi}\left(Q_K^s\right)+\sum_{K=1}^{L}\phi_K^{uq}(x^v,y^v,z^v,n^v)\widehat{q}\left(Q_K^s\right), \tag{3}$$

$$q\left(Q_j^v\right)=\sum_{K=1}^{L}\phi_K^{qu}(x^v,y^v,z^v)\widehat{\phi}\left(Q_I^s\right)+\sum_{K=1}^{L}\phi_K^{qq}(x^v,y^v,z^v,n^v)\widehat{q}\left(Q_K^s\right), \tag{4}$$

where L are the number of source nodes close to the virtual nodeQ_j^v, (x^v,

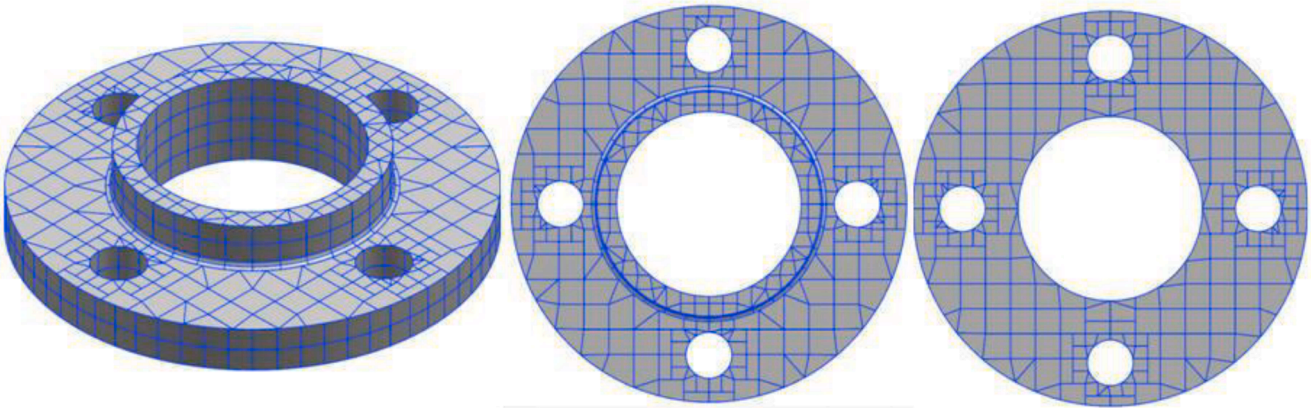

Fig. 2. Binary tree grids of flange.

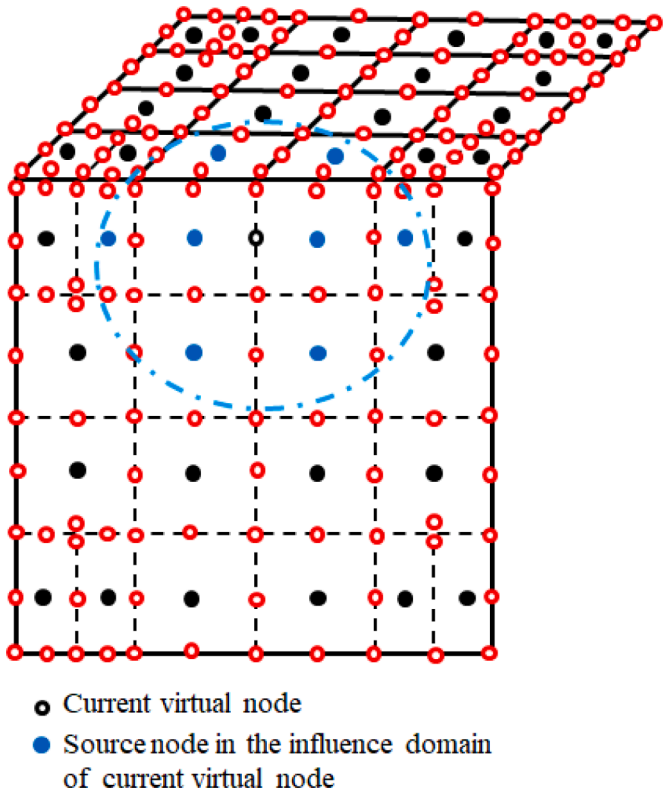

Fig. 3. Implementation diagram of the Second-layer interpolation.

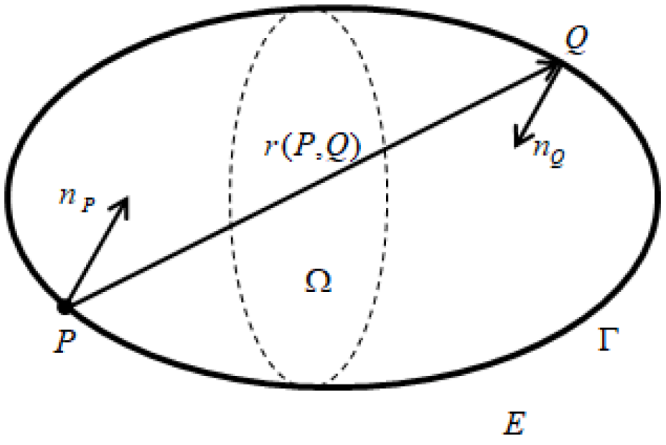

Fig. 4. The acoustic medium ***E***, body$\Omega$and its boundaryΓ.

y^v,z^v)andn^vrepresent the Cartesian coordinates and the outward normal, respectively. $\phi_K^{uu}(x^v,y^v,z^v)$,$\phi_K^{uq}(x^v,y^v,z^v,n^v)$, $\phi_K^{qu}(x^v,y^v,z^v)$, and $\phi_K^{qq}(x^v,y^v,z^v,n^v)$ represent the shape functions of HMLS approximation and their forms are given below:

$$\phi_I^{uu}(x^v,y^v,z^v)=\mathbf{p}_u^T(x^v,y^v,z^v)\mathbf{C}^{-1}\mathbf{P}_u\left(x_I^s,y_I^s,z_I^s\right)w_I(x^v,y^v,z^v), \tag{5}$$

$$\phi_I^{uq}(x^v,y^v,z^v)=\mathbf{p}_u^T(x^v,y^v,z^v)\mathbf{C}^{-1}\mathbf{P}_q\left(x_I^s,y_I^s,z_I^s,n_I^s\right)w_I(x^v,y^v,z^v), \tag{6}$$

$$\phi_I^{qu}(x^v,y^v,z^v)=\mathbf{p}_q^T(x^v,y^v,z^v,n^v)\mathbf{C}^{-1}\mathbf{P}_u\left(x_I^s,y_I^s,z_I^s\right)w_I(x^v,y^v,z^v), \tag{7}$$

$$\phi_I^{qq}(x^v,y^v,z^v)=\mathbf{p}_q^T(x^v,y^v,z^v,n^v)\mathbf{C}^{-1}\mathbf{P}_q\left(x_I^s,y_I^s,z_I^s,n_I^s\right)w_I(x^v,y^v,z^v), \tag{8}$$

where

$$\mathbf{C}=\mathbf{P}_u^T\mathbf{W}\mathbf{P}_u+\mathbf{P}_q^T\mathbf{W}\mathbf{P}_q, \tag{9}$$

$$\mathbf{W}=\begin{bmatrix} w_1 & 0 & \cdots & 0 \\ 0 & w_2 & \cdots & 0 \\ \vdots & \vdots & \ddots & \vdots \\ 0 & 0 & \cdots & w_M \end{bmatrix}, \tag{10}$$

$$\mathbf{P}_u^{\mathrm{T}}=\left[\mathbf{p}_u(x_1,y_1,z_1)\quad \mathbf{p}_u(x_2,y_2,z_2)\quad \cdots\quad \mathbf{p}_u(x_M,y_M,z_M)\right], \tag{11}$$

$$\mathbf{P}_q^{\mathrm{T}}=\left[\mathbf{p}_q(x_1,y_1,z_1,n_1)\quad \mathbf{p}_q(x_2,y_2,z_2,n_2)\quad \cdots\quad \mathbf{p}_q(x_M,y_M,z_M,n_M)\right], \tag{12}$$

where $\mathbf{p}_u$ and $\mathbf{p}_q$ indicate the basis vectors for sound pressure ϕ and sound flux q, respectively. $w_I(x^v,y^v,z^v)$ represents the weight function.

3. DiBFM for 3-D acoustic problems

3.1. Basic equations in acoustics

Consider an acoustic problem with homogeneous medium as shown in Fig. 4, the Helmholtz equation and BCs are given as [19]:

$$\begin{aligned} &\nabla^2\phi+k^2\phi=0,\forall\mathbf{x}\in E\\ &\phi=\overline{\phi},\forall\mathbf{x}\in\Gamma_D\\ &q=\frac{\partial\phi}{\partial n}=\overline{q}=i\omega\rho v_n,\forall\mathbf{x}\in\Gamma_N\\ &\phi=Zv_n,\forall\mathbf{x}\in\Gamma_R \end{aligned}, \tag{13}$$

where E is the acoustic medium, Ω and Γ are the body and its boundary. Γ_D,Γ_N and Γ_R denote the Dirichlet, Neumann and Robin boundaries, respectively. i is the imaginary unit, n represents the unit normal. ρ,ω, v_n and k denote the mass density, circular frequency, normal velocity and wave number, respectively. Z is the impedance.

The CBIE for acoustic problems is given [20]:

$$c(P)\phi(P)=\int_\Gamma G(P,Q)q(Q)d\Gamma(Q)-\int_\Gamma F(P,Q)\phi(Q)d\Gamma(Q)+\phi^I(P), \tag{14}$$

where P is the source point and Q denotes the field point, $c(P)$ is the constant coefficient related to the boundary situation at point P. $\phi^I(P)$ represents the incident wave for scattering problems. $G(P, Q)$ and $F(P, Q)$ are the kernel functions, for 3-D acoustic problems, they have the forms as follows

$$G(P,Q)=\frac{1}{4\pi r}e^{ikr}, \tag{15}$$

$$F(P,Q)=\frac{\partial G(P,Q)}{\partial n(Q)}=\frac{1}{4\pi r^2}(ikr-1)r_{,j}n_j(Q)e^{ikr}, \tag{16}$$

where r represents the distance between P and Q, and $r,_j=\partial r/\partial Q_j=(P_j-Q_j)/r$, $j=1, 2, 3$, n_j is the component of normal n.

3.2. Burton-Miller formulation

It's well known that there is the fictitious eigenfrequency problem [5] when applying the CBIE method to solve exterior acoustics problems. An effective approach to solve this problem is to use the Burton-Miller formulation which coupling the CBIE with its normal derivative. Taking the derivative of the CBIE with respect to the normal at the source point P, the hypersingular boundary integral equation (HBIE) can be obtained as below:

$$\widetilde{c}(P)q(P)=\int_\Gamma K(P,Q)q(Q)d\Gamma(Q)-\int_\Gamma H(P,Q)\phi(Q)d\Gamma(Q)+q^I(P), \tag{17}$$

where

$$K(P,Q)=\frac{\partial G(P,Q)}{\partial n(P)}=-\frac{1}{4\pi r^2}(ikr-1)r_{,j}n_j(P)e^{ikr}, \tag{18}$$

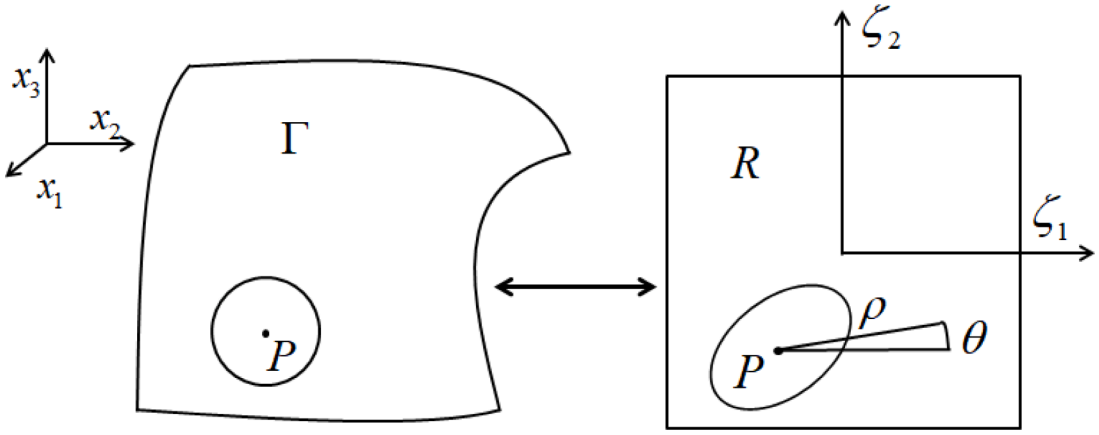

Fig. 5. Mapping diagram between the Cartesian coordinates and intrinsic coordinates.

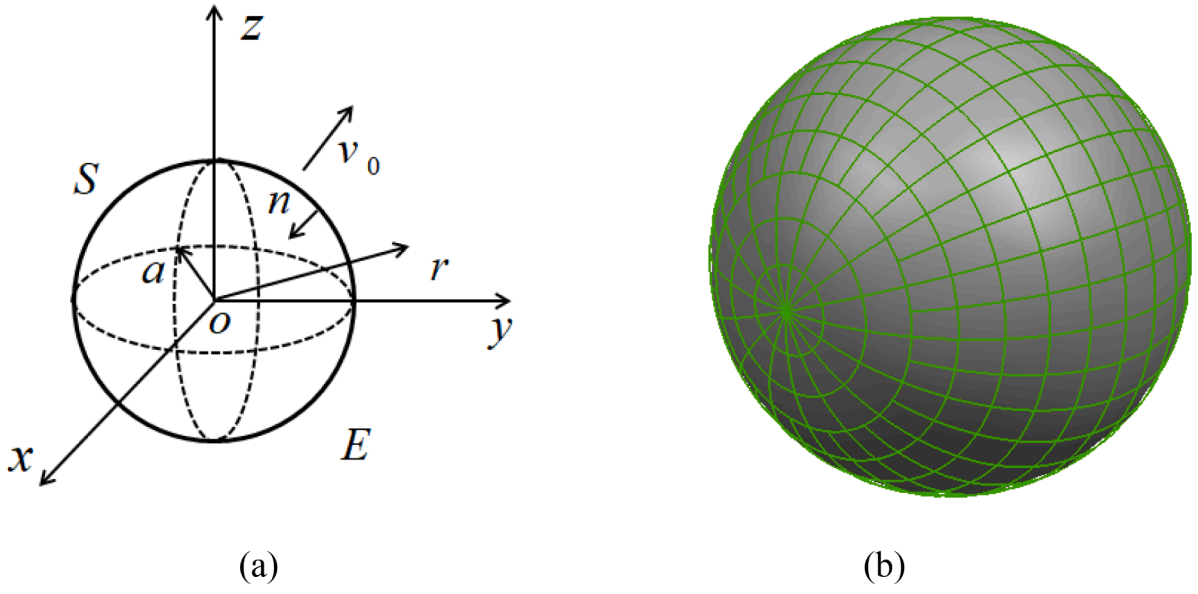

Fig. 6. (a) a pulsating sphere in an infinite medium E and (b) its binary tree grids with 416 elements.

Table 1
Comparison of relative error and CPU time between DiBFM and conventional BEM.

DiBFM			Conventional **BEM**		
Ns	*Err_u*	*Time(s)*	*Ns*	*Err_u*	*Time(s)*
288	1.213E-3	137	288	2.48E-2	82
416	7.250E-4	285	416	2.07E-2	170
928	2.206E-4	396	928	1.65E-2	227
1344	1.955E-4	803	1344	1.37E-2	456

$$H(P,Q)=\frac{\partial F(P,Q)}{\partial n(P)}=\frac{1}{4\pi r^3}\left\{(1-ikr)n_j(Q)+\left[k^2r^2-3(1-ikr)\right]r_{,j}r_{,l}n_l(Q)\right\}n_j(P)e^{ikr}, \tag{19}$$

Coupling Eq. (14) with Eq. (17), the Burton-Miller formulation can be written as:

$$CBIE+\beta HBIE=0, \tag{20}$$

where β is a complex number called the coupling constant, and the choice of the coupling constant depends on both the time-dependent term and the problem type, relevant studies can be found in [21–22]. In this paper, $\beta=i/k$is taken.

Since the strongly singular and hypersingular integrals are introduced in Eq. (17), the effective calculation of these integrals becomes a new challenge. Based on the Cauchy principal value and Hadamard finite part integrals, regularization [9] and local coordinate approximate expansion [8] are employed to handle these integrals as follows:

$$\begin{aligned}&\int_\Gamma K(P,Q)N^a d\Gamma(Q)=\int_\Gamma (K(P,Q)-\overline{F}(P,Q))N^a d\Gamma(Q)+\int_\Gamma \overline{F}(P,Q)N^a d\Gamma(Q)\\&=\int_R\int (K(P,Q)-\overline{F}(P,Q))N^a J d\zeta_1 d\zeta_2+\int_R\int \overline{F}(P,Q)N^a J d\zeta_1 d\zeta_2\\&=\int_R\int (K(P,Q)-\overline{F}(P,Q))N^a J\rho d\rho d\theta+\int_R\int \overline{F}(P,Q)N^a J\rho d\rho d\theta\\&=o(1),as\rho\to 0,\end{aligned} \tag{21}$$

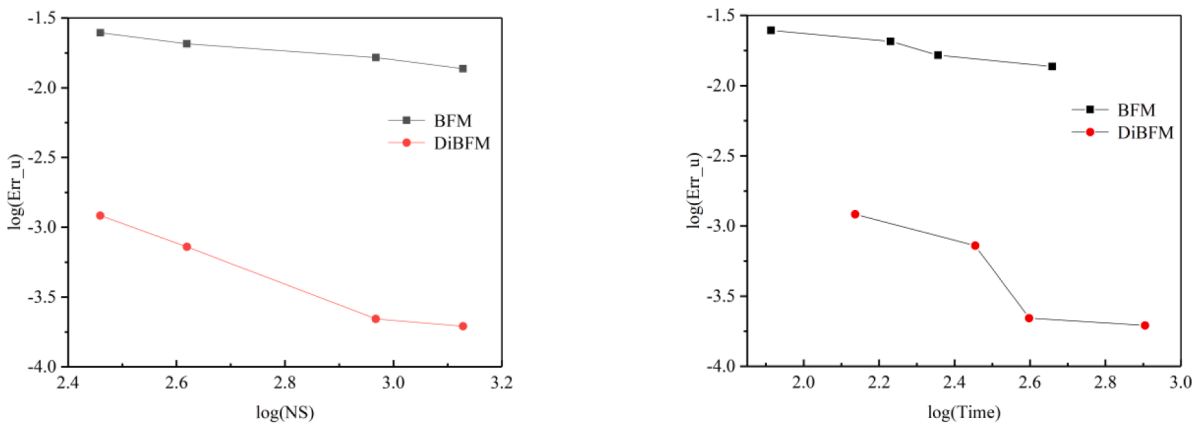

Fig. 7. Comparison of accuracy and efficiency between DiBFM and conventional BEM.

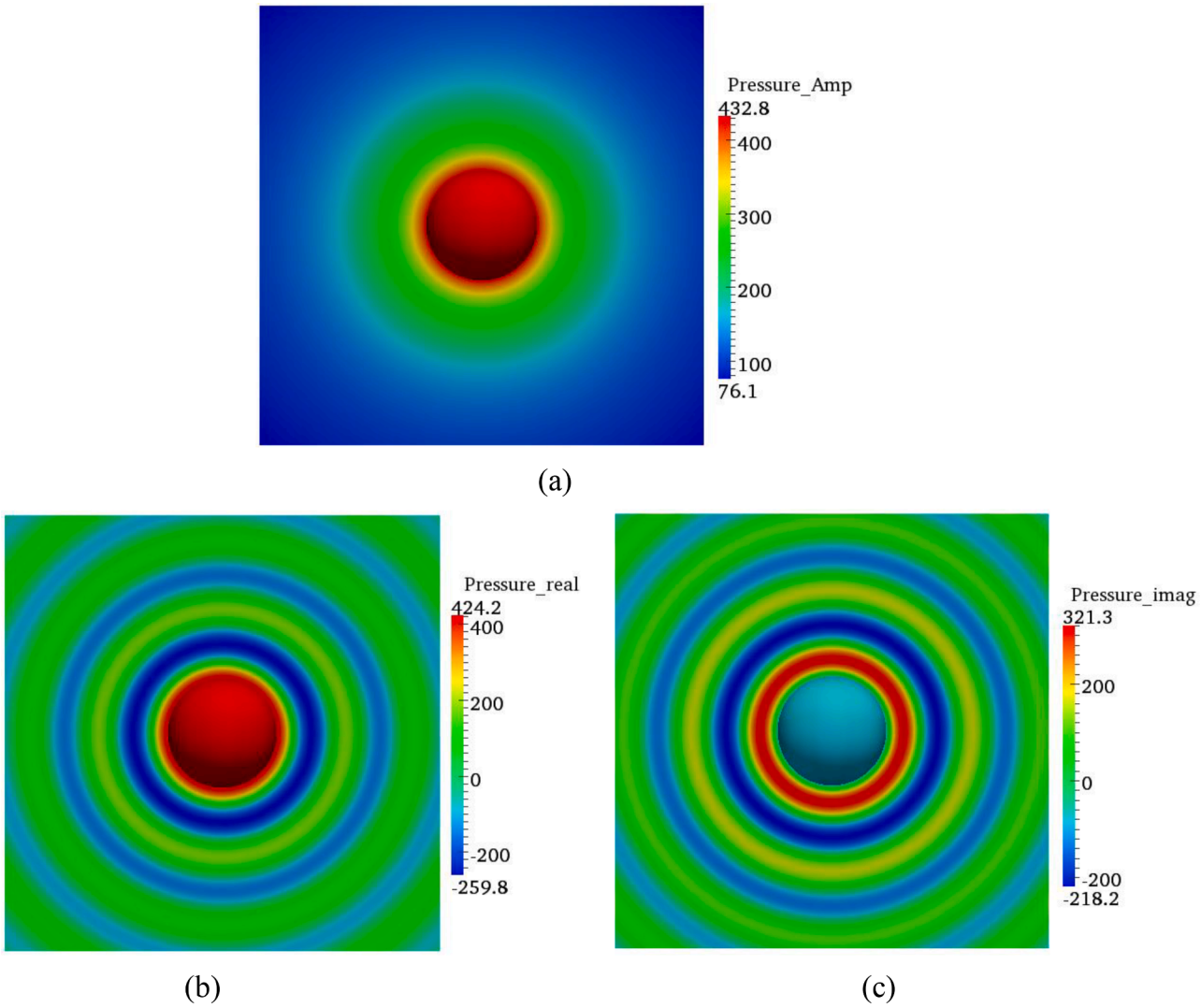

Fig. 8. Contours of (a) amplitude, (b) real part and (c) imaginary part of sound pressure.

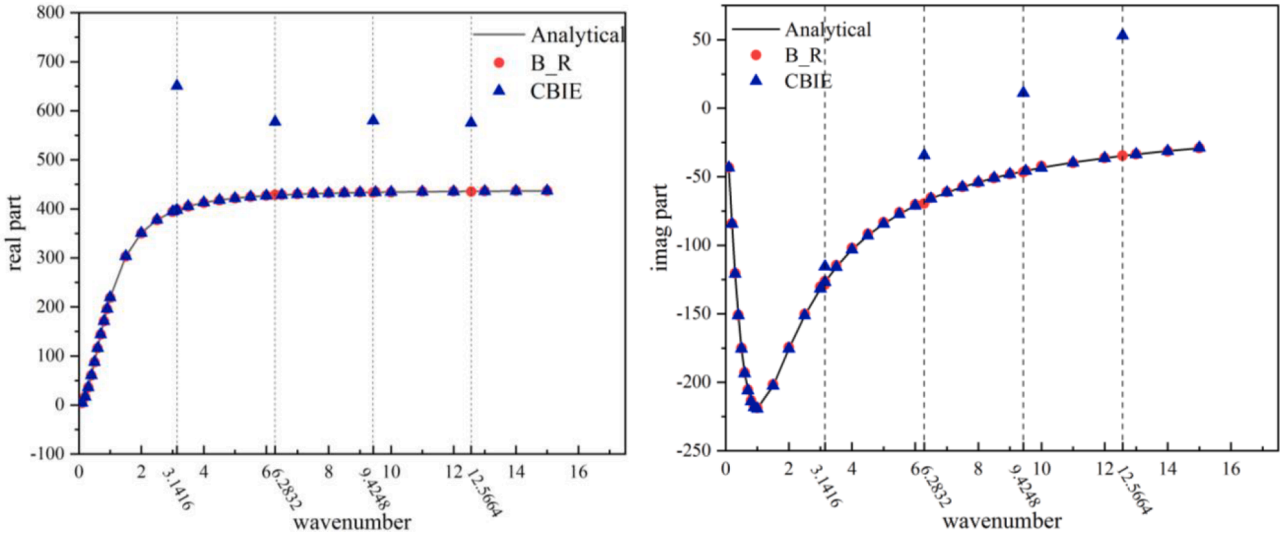

Fig. 9. The solutions of sound pressure for boundary point at different wavenumbers.

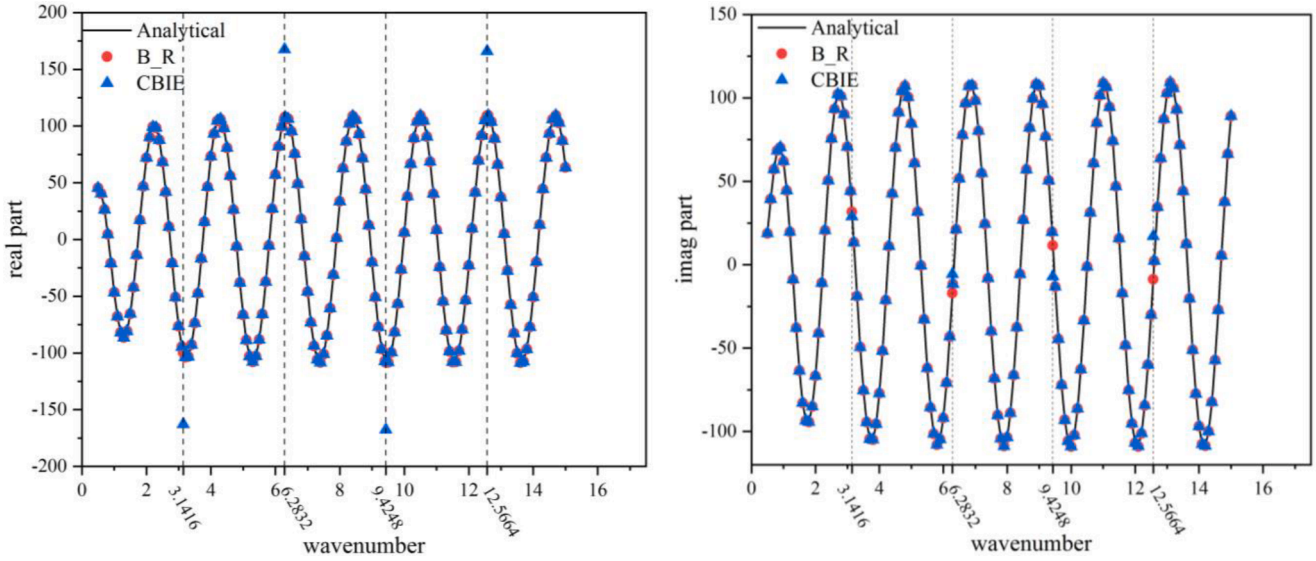

Fig. 10. The solutions of sound pressure for field point at different wavenumbers.

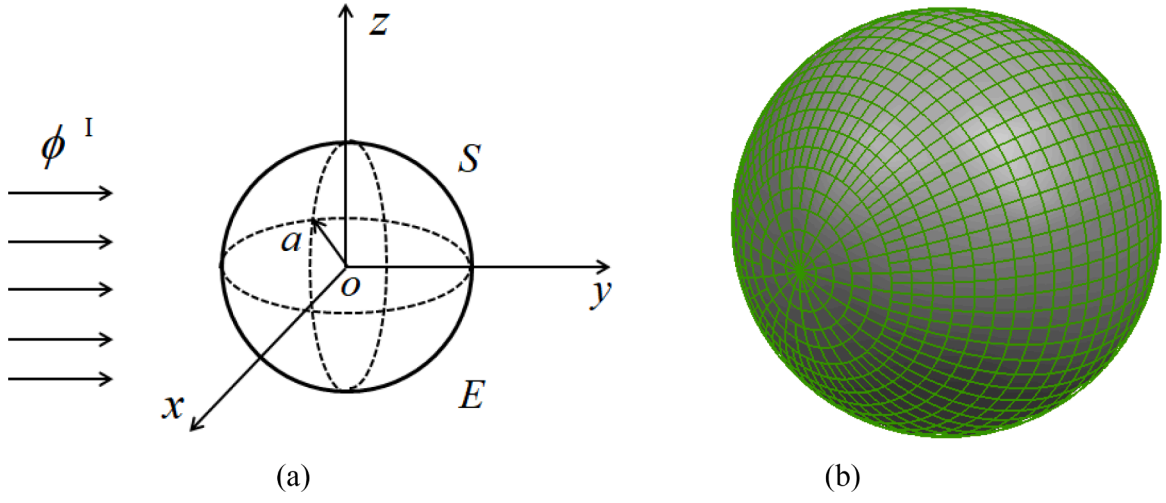

Fig. 11. (a) A rigid sphere impinged by plane wave and (b) its binary grids with 1632 elements.

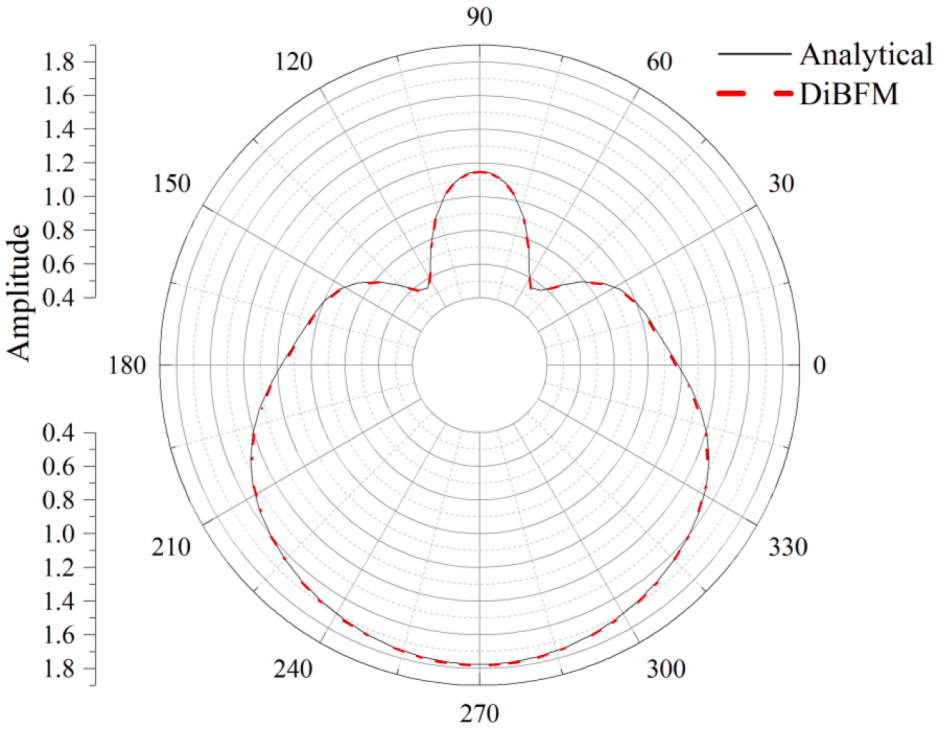

Fig. 12. The polar diagram of pressure amplitude at points on x-y plane.

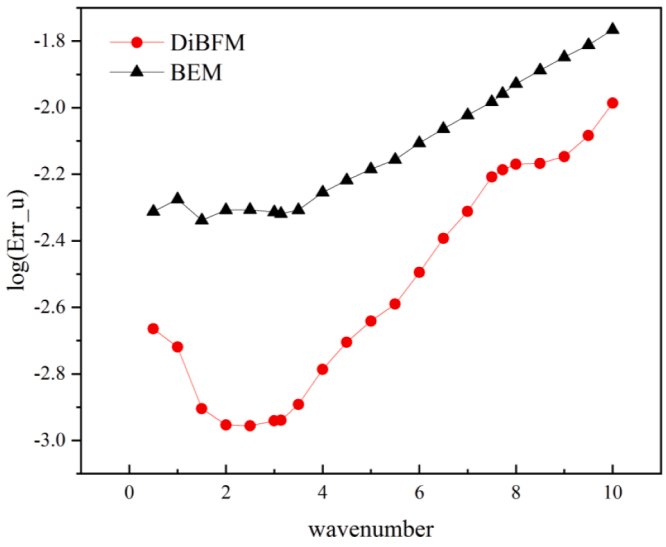

Fig. 13. The relative errors of sound pressure amplitude at boundary points.

$$\begin{aligned}&\int_\Gamma H(P,Q)N^a d\Gamma(Q)=\int_\Gamma (H(P,Q)+\overline{H}(P,Q))N^a d\Gamma(Q)-\int_\Gamma \overline{H}(P,Q)N^a d\Gamma(Q)\\&=\int_R\int (H(P,Q)+\overline{H}(P,Q))N^a J d\zeta_1 d\zeta_2-\int_R\int \overline{H}(P,Q)N^a J d\zeta_1 d\zeta_2\\&=\int_R\int (H(P,Q)+\overline{H}(P,Q))N^a J\rho d\rho d\theta-\int_R\int \overline{H}(P,Q)N^a J\rho d\rho d\theta\\&=o\left(\rho^{-2}\right)+o\left(\rho^{-1}\right)+o(1), as\rho\to 0,\end{aligned} \tag{22}$$

where (ζ_1,ζ_2) and (ρ, θ) are the intrinsic and polar coordinates as shown in Fig. 5, respectively. J is the jacobian of transformation between the Cartesian and intrinsic coordinates, N^a represents the shape function at the a^{th}interpolation point. $\overline{F}(P,Q)$ and $\overline{H}(P,Q)$denote the kernel functions of potential problems in three-dimension, and they have the forms below:

$$\overline{F}(P,Q)=-\frac{1}{4\pi r^2}r_{,j}n_j(Q), \tag{23}$$

$$\overline{H}(P,Q)=\frac{1}{4\pi r^3}\left[n_l(P)n_l(Q)-3r_{,j}n_j(P)r_{,l}n_l(Q)\right], \tag{24}$$

The singular integrals in the Eq. (21) can be handled readily by numerical integration and that in Eq. (22) also can be calculated accurately by introducing the Cauchy principal value and Hadamard finite part integrals.

3.3. Discretization

Substituting Eq. (1) into the Eq. (20), the discretized equation of Burton-Miller formulation using dual interpolation elements can be written as:

$$\begin{aligned}&\sum_{e=1}^{ne}\left[\sum_{i=1}^{ni}h^{ss}(P_k)\phi\left(Q^s_{e(i)}\right)+\sum_{j=1}^{nj}h^{sv}(P_k)\phi\left(Q^v_{e(j)}\right)\right]\\&=\sum_{e=1}^{ne}\left[\sum_{i=1}^{ni}g^{ss}(P_k)q\left(Q^s_{e(i)}\right)+\sum_{j=1}^{nj}g^{sv}(P_k)q\left(Q^v_{e(j)}\right)\right]+b^I(P_k),\end{aligned} \tag{25}$$

in which

$$\begin{aligned}h^{ss}(P_k)=&\int_{\Gamma_e}\frac{\partial G(P,Q)}{\partial n(Q)}N^s_{e(i)}(Q)d\Gamma(Q)+\beta\int_{\Gamma_e}\frac{\partial^2 G(P,Q)}{\partial n(P)\partial n(Q)}N^s_{e(i)}(Q)d\Gamma(Q)\\&+\frac{1}{2}\delta^k_{e(i)},\end{aligned} \tag{26}$$

$$h^{sv}(P_k)=\int_{\Gamma_e}\frac{\partial G(P,Q)}{\partial n(Q)}N^v_{e(j)}(Q)d\Gamma(Q)+\beta\int_{\Gamma_e}\frac{\partial G^2(P,Q)}{\partial n(P)\partial n(Q)}N^v_{e(j)}(Q)d\Gamma(Q), \tag{27}$$

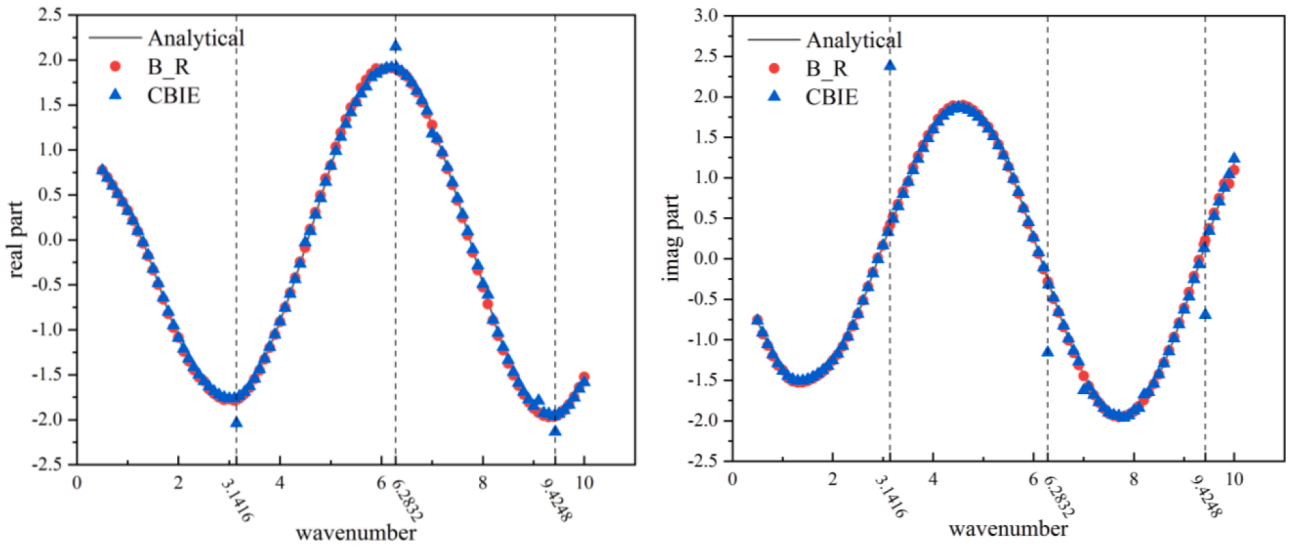

Fig. 14. The solutions of sound pressure for boundary point at different wavenumbers.

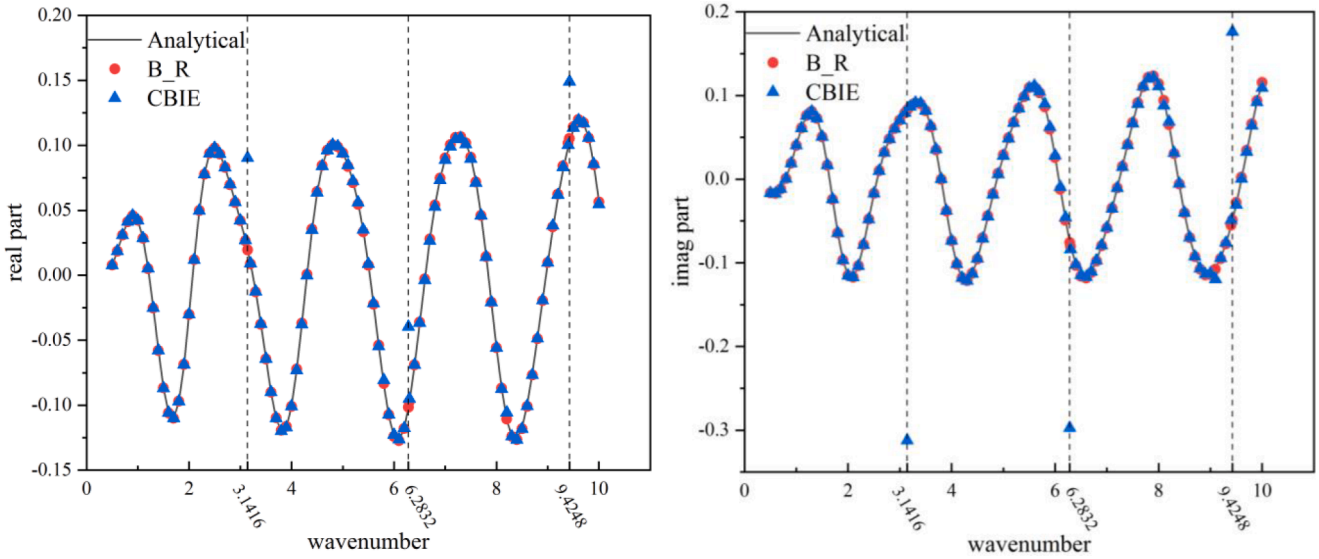

Fig. 15. The solutions of sound pressure for field point at different wavenumbers.

$$g^{ss}(P_k)=\int_{\Gamma_e} G(P,Q)N^s_{e(i)}(Q)d\Gamma(Q)-\beta\left[\int_{\Gamma_e}\frac{\partial G(P,Q)}{\partial n(P)}N^s_{e(i)}(Q)d\Gamma(Q)-\frac{1}{2}\delta^k_{e(i)}\right], \tag{28}$$

$$g^{sv}(P_k)=\int_{\Gamma_e} G(P,Q)N^v_{e(j)}(Q)d\Gamma(Q)+\int_{\Gamma_e}\frac{\partial G(P,Q)}{\partial n(P)}N^v_{e(j)}(Q)d\Gamma(Q), \tag{29}$$

$$b^I(P_k)=\phi^I(P_k)+\beta q^I(P_k), \tag{30}$$

and

$$\delta^k_{e(i)}=\begin{cases}1, & \text{if } \mathrm{P}_k \text{ is the } i^{\text{th}} \text{ source node in } e^{\text{th}} \text{ element}\\ 0\end{cases}, \tag{31}$$

where P_k represents k^{th} source point ($k = 1, 2, \ldots, ns$). *ns, ne*denote the number of total sources points and elements, *ni, nj* represent the number of the source and virtual points in an element, respectively. The superscript "*s*" and "*v*" indicate the source and virtual point, respectively. In matrix form, Eq. (25) can be written in following:

$$\mathbf{Hu}=\mathbf{Gq}+\mathbf{b}^I, \tag{32}$$

where **u** and **q** are the vectors of sound pressure and sound flux, respectively. **H** and **G** denote the coefficient matrices and $\mathbf{b}^I$ is the right vector obtained by incident wave in scattering problem.

3.4. Assembly and solution

Considering the source and virtual points separately in Eq. (32):

$$[\mathbf{H}^{ss}\quad \mathbf{H}^{sv}]\begin{Bmatrix}\mathbf{u}^s\\ \mathbf{u}^v\end{Bmatrix}=[\mathbf{G}^{ss}\quad \mathbf{G}^{sv}]\begin{Bmatrix}\mathbf{q}^s\\ \mathbf{q}^v\end{Bmatrix}+\mathbf{b}^I, \tag{33}$$

where

$$\mathbf{u}^{\mathrm{v}}=\overline{\mathbf{u}}^{\mathrm{v}}+\widehat{\mathbf{u}}^{\mathrm{v}}, \tag{34}$$

$$\mathbf{q}^{\mathrm{v}}=\overline{\mathbf{q}}^{\mathrm{v}}+\widehat{\mathbf{q}}^{\mathrm{v}}, \tag{35}$$

where the superscript '– ' and '^' indicate the specified and unknown quantities, respectively. Applying Eqs. (3-4), we obtain:

$$\widehat{\mathbf{u}}^{\mathrm{v}}=\mathbf{\Phi}^{vs}_{uu}\mathbf{u}^s+\mathbf{\Phi}^{vs}_{uq}\mathbf{q}^s, \tag{36}$$

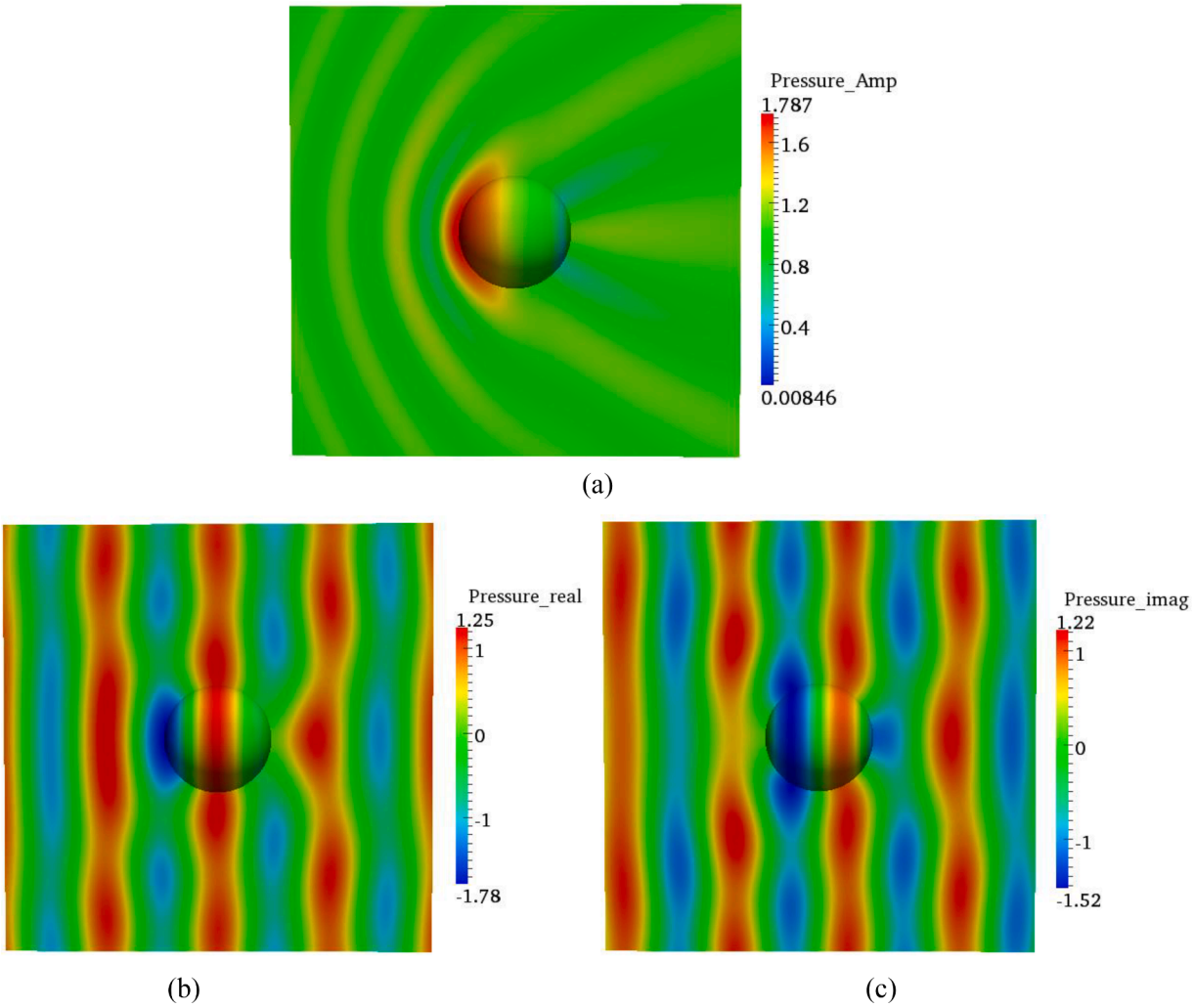

Fig. 16. Contours of (a) amplitude, (b) real part and (c) imaginary part of sound pressure.

$$\widehat{\mathbf{q}}^{v} = \mathbf{\Phi}_{qu}^{vs}\mathbf{u}^{s} + \mathbf{\Phi}_{qq}^{vs}\mathbf{q}^{s}, \tag{37}$$

where $\mathbf{\Phi}_{uu}^{vs}$, $\mathbf{\Phi}_{uq}^{vs}$, $\mathbf{\Phi}_{qu}^{vs}$, and $\mathbf{\Phi}_{qq}^{vs}$ represent the shape functions defined in Section 2.2.

Substituting Eqs. (33-37) into Eq. (32), we have:

$$\mathbf{H}^{s}\mathbf{u}^{s} = \mathbf{G}^{s}\mathbf{q}^{s} + \mathbf{b}^{v}, \tag{38}$$

where

$$\mathbf{H}^{s} = \mathbf{H}^{ss} + \mathbf{H}^{sv}\mathbf{\Phi}_{uu}^{vs} - \mathbf{G}^{sv}\mathbf{\Phi}_{qu}^{vs}, \tag{39}$$

$$\mathbf{G}^{s} = \mathbf{G}^{ss} + \mathbf{G}^{sv}\mathbf{\Phi}_{qq}^{vs} - \mathbf{H}^{sv}\mathbf{\Phi}_{uq}^{vs}, \tag{40}$$

$$\mathbf{b}^{v} = -\mathbf{H}^{sv}\overline{\mathbf{u}}^{v} + \mathbf{G}^{sv}\overline{\mathbf{q}}^{v} + \mathbf{b}^{I}, \tag{41}$$

Applying the BCs, Eq. (38) yields:

$$\{\overline{\mathbf{H}}^{s} \quad \widehat{\mathbf{H}}^{s}\}\begin{Bmatrix}\overline{\mathbf{u}}^{s}\\ \widehat{\mathbf{u}}^{s}\end{Bmatrix} = \{\overline{\mathbf{G}}^{s} \quad \widehat{\mathbf{G}}^{s}\}\begin{Bmatrix}\overline{\mathbf{q}}^{s}\\ \widehat{\mathbf{q}}^{s}\end{Bmatrix} + \mathbf{b}^{v}, \tag{42}$$

With relocation, we have:

$$\mathbf{A}\mathbf{x} = \mathbf{b}, \tag{43}$$

where

$$\mathbf{A} = \{\widehat{\mathbf{H}}^{s} \quad \widehat{\mathbf{G}}^{s}\}, \mathbf{x} = \begin{Bmatrix}\widehat{\mathbf{u}}^{s}\\ \widehat{\mathbf{q}}^{s}\end{Bmatrix}, \mathbf{b} = \overline{\mathbf{G}}^{s}\overline{\mathbf{q}}^{s} + \mathbf{b}^{v} - \overline{\mathbf{H}}^{s}\overline{\mathbf{u}}^{s} + \mathbf{b}^{I}, \tag{44}$$

in which **A** is the system matrix, **x** is the vector of unknown variables only at the source nodes, and **b** is the known vector containing contributions from boundary conditions.

The scale of Eq. (43) is the same as that of conventional BEM, however, the proposed method can obtain better accuracy and efficiency by imposing the boundary conditions more precisely and increasing the interpolation precision.

4. Numerical examples

Three numerical examples are presented to illustrate the superiority of the proposed method in this section. The two typical examples in acoustic problem, radiation and scattering problems of unit sphere are presented to show its accuracy and efficiency. The last example is given to demonstrate its capacity to handle complex model. Analytical or commercial software solutions are compared with the solutions obtained by the DiBFM. The relative error is defined below:

$$error = \frac{1}{|w^{(e)}|_{\max}}\sqrt{\frac{1}{L}\sum_{i=1}^{L}\left[w_i^{(e)} - w_i^{(n)}\right]^2}, \tag{45}$$

where $|w^{(e)}|_{\max}$ represents the maximum value of sound pressure among L sample points, $w_i^{(e)}$ and $w_i^{(n)}$ are the reference and numerical results, respectively. Symbols *Err_u* indicate the relative error of sound pressure amplitude ϕ and *Time* the total CPU time, and *NS* represents the number

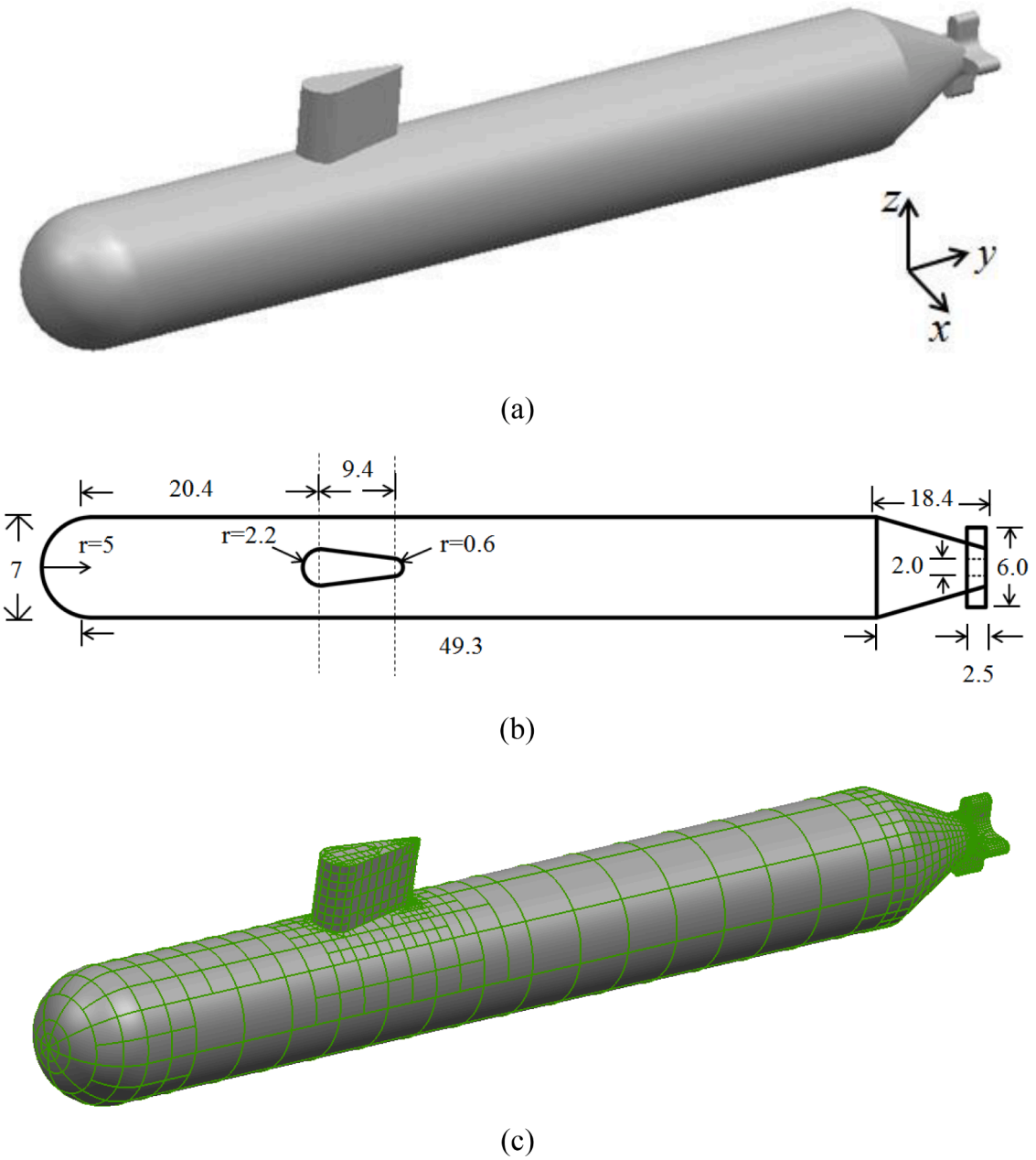

Fig. 17. (a) Geometry of submarine and (b) its size and (c) its binary tree grids with 3382 elements.

of source nodes.

4.1. Radiation from a pulsating sphere

In the pulsating sphere problem, a=1 m is the radius and $v_0 = 1m/s$ is the constant radial velocity which is prescribed over the surface of sphere as shown in Fig. 6(a). The analytical solution of sound pressure at a given point of radius r can be obtained by [23]:

$$\phi(r,k) = \frac{\rho c v_0 (ika)}{ika - 1} \frac{a}{r} e^{ik(r-a)}, \tag{46}$$

where k is the wavenumber, ρ and c denote the mass density and speed of sound, respectively.

In this case, $\rho = 1.29kg/m^3$ and $c = 340m/s$ are used, and the boundaries are discretized with 416 constant elements as shown in Fig. 6 (b).

Considering a point located on the sphere, the relative errors of sound pressure amplitude and CPU time are presented in Table 1.

Examining Table 1 and Fig. 7 reveals that the DiBFM can achieve higher accuracy than Tradition BEM when using the same number of source nodes, and takes less time than Tradition BEM at the same error level.

Fig. 8 shows the distribution of sound pressure in a square area obtained by DiBFM, the sound pressure at any point is only related to the polar diameter, which is consistent with the law of radiation from the pulsating sphere.

To verify the validity of the DiBFM with Burton–Miller formulation for radiation problems, the boundary point at (1, 0, 0) and the field point at (4, 0, 0) are selected as the sample points, and their results of sound pressure with changing wavenumbers $k \in (0, 15]$ are given in Fig. 9 and 10, respectively, Symbols 'B_R' and 'CBIE' represent the DiBFM using Burton–Miller formulation and CBIE respectively.

It can be seen from the above figures, the results obtained by the DiBFM with Burton–Miller formulation agree well with analytical

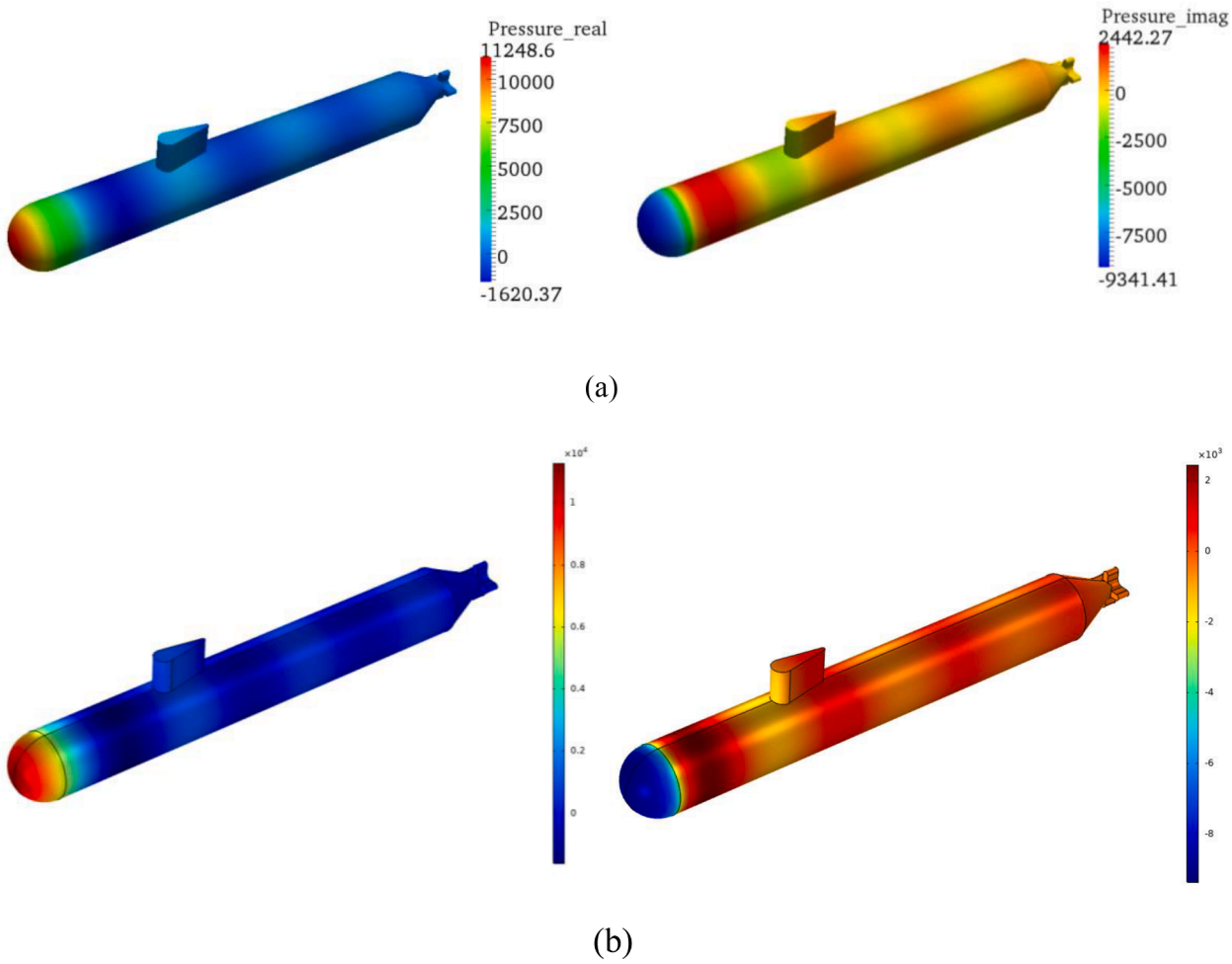

Fig. 18. The distributions of sound pressure in radiation problem: (a) DiBFM, (b) commercial software.

Table 2
Relative errors between DiBFM and software in radiation problem.

	real part			imag part		
	DiBFM	Software	*Err*	DiBFM	Software	*Err*
Maximum value	11,248.6	11,263.2	0.13%	2442.27	2439.05	0.13%
Minimum value	−1620.37	−1619.89	0.03%	−9341.41	−9361.24	0.21%

solutions at given wavenumbers, and there is no fictitious eigenfrequency phenomenon.

4.2. Scattering from a rigid sphere

The scattering problem of the rigid sphere is studied next. As shown in Fig. 11(a), the rigid sphere with radius $a = 1$ m is impinged by the plane wave. The plane wave with unit amplitude propagating alone the y axis is considered, and the incident sound pressure at a point in the sound field is given by:

$$\phi_i = \phi_0 e^{ik\mathbf{x}\cdot\overrightarrow{d}}, \tag{47}$$

where $\mathbf{x}$is the Cartesian coordinates of the field point, $\phi_0 = 1Pa$and $\overrightarrow{d} = (0,\ 1,\ 0)$are the amplitude and direction vector of plane wave, respectively.

For a rigid sphere impinged by plane wave, the analytic solution of scattering sound pressure is given as follows [23]:

$$\phi_s = -p_0 \sum_{n=0}^{\infty} i^n (2n+1) \frac{nj_{n-1}(ka) - (n+1)j_{n+1}(ka)}{nh_{n-1}^{(1)}(ka) - (n+1)h_{n+1}^{(1)}(ka)} h_n^{(1)}(kr) P_n(cos\theta), \tag{48}$$

where r, θ are the polar coordinates of the field point, P_n denotes the Legendre function, and$j_n, h_n^{(1)}$ are the spherical Bessel function and Hankel function of the first kind, respectively.

In this case, $\rho = 1.29kg/m^3$ and $c = 340m/s$ are also used, and the boundaries are discretized with 1632 constant elements as shown in Fig. 11 (b).

Taking the points where the sphere intersects the x-y plane as the sample points and the wavenumber $k = 5$ is used, the solution of sound pressure amplitude is given in Fig. 12, and the relative errors of sound pressure amplitude with changing wavenumbers $k \in (0, 10]$ at boundary points are presented in Fig. 13.

Fig. 12 shows the result obtained by the DiBFM are highly consistent with analytical solution, and Fig. 13 reveals that the error mainly increases with the increase of wavenumber, and the results obtained by the DiBFM have less error than that obtained by Tradition BEM.

Also to verify the validity of the DiBFM with Burton–Miller

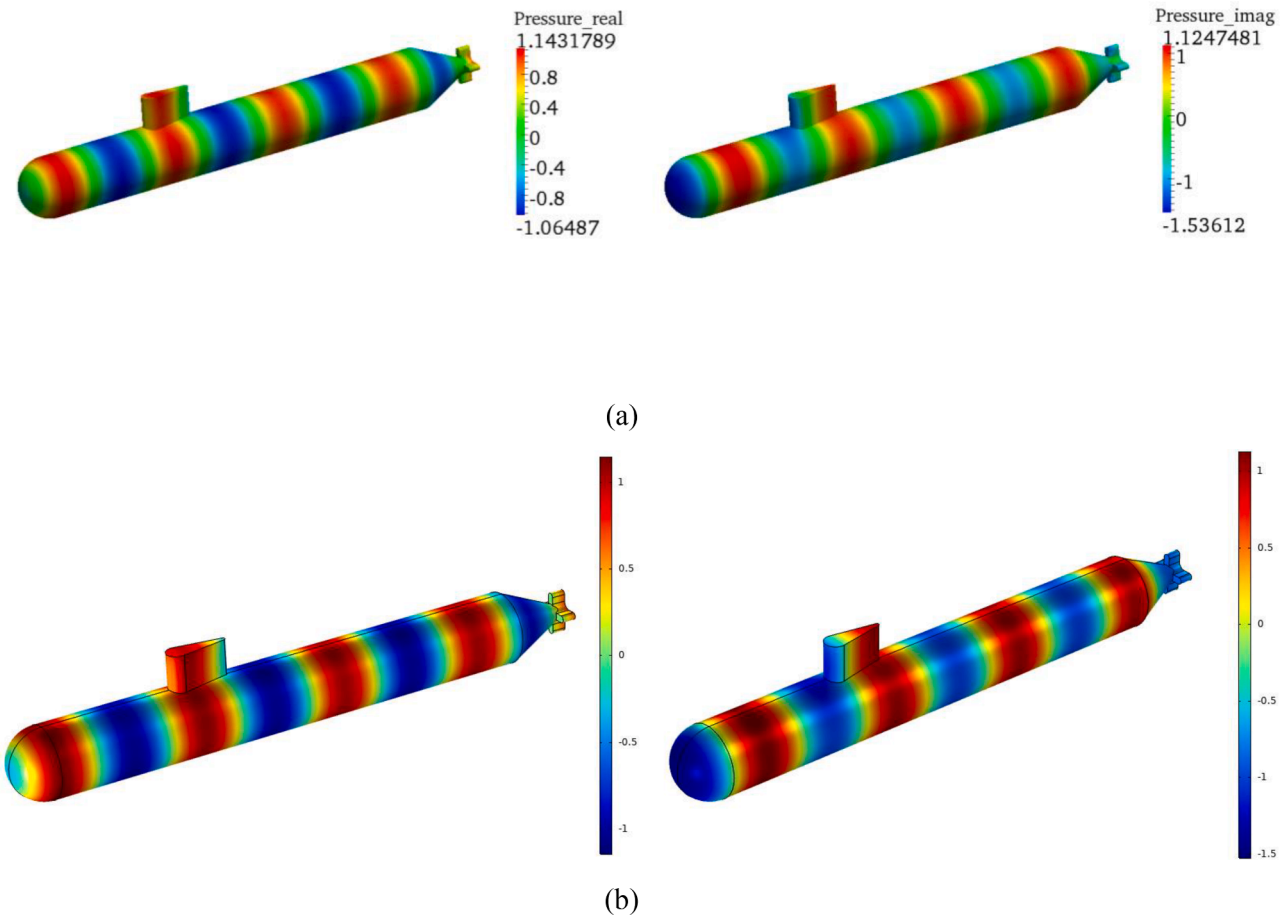

Fig. 19. The distributions of sound pressure in scattering problem: (a) DiBFM, (b) commercial software.

Table 3
Relative errors between DiBFM and software in scattering problem.

	real part			imag part		
	DiBFM	Software	*Err*	DiBFM	Software	*Err*
Maximum value	1.143789	1.14638	0.23%	1.124748	1.12593	0.10%
Minimum value	−1.06487	−1.06685	0.19%	−1.53612	−1.52506	0.73%

formulation for scattering problems, the boundary point at (0, −1, 0) and the field point at (4, 0, 0) are selected as the sample points, and their results of sound pressure with changing wavenumbers $k \in (0, 10]$ are given in Fig. 14 and 15, respectively.

Figs. 14 and 15 reveal that the solutions obtained by the DiBFM are in line with analytical solutions at given wavenumbers. Fig. 16 shows the scattering phenomenon of external sound field .This example illustrates the effectiveness of the proposed method for scattering problems.

4.3. Submarine

To demonstrate the ability of the DiBFM to handle complex geometry, the submarine is investigated in this case and it is discretized with 3382 elements, as shown in Fig. 17. Since the sound filed medium changes from air to water, $\rho = 1000kg/m^3$ and $c = 1500m/s$ are used. The results of commercial software would be selected as reference solutions.

Considering the radiation problem from the submarine firstly, the velocity boundary condition $v_n = 0.01m/s$is applied on the hemisphere face. The distributions of sound pressure at wavenumber $k = 3$ are given in Fig. 18, and Table 2 presents the relative error between the DiBFM and commercial software.

It can be seen from the Fig. 18 and Table 2, the results obtained by the DiBFM are almost consistent with that obtained by commercial software while the style of the legend is different, the relative errors of maximum and minimum value are less than 0.3%. This example shows the ability of the DiBFM to solve the radiation problem of complex model.

Next, the scattering problem that a unit amplitude incident wave impinged on the submarine from the direction $\vec{d}(0, 1, 0)$ is taken into account, the model configurations are same with above case.

The distribution of sound pressure are presents in Fig. 19, the solutions given by the DiBFM are consistent with that obtained by commercial software, Table 3 shows the relative errors of maximum and minimum value are below 1%, this example shows the ability of the DiBFM to solve the scattering problem of complex model.

5. Conclusions

Based on the binary tree grids, the DiBFM has been developed to solve 3-D exterior acoustic problems. The binary tree grids include continuous and discontinuous grids, which makes mesh generation of

arbitrary models more automatic. The DiBFM using binary tree grids makes full use of the property that the trail function of BIE does not need to be continuous. By implementing the dual interpolation elements in the DiBFM, the interpolation accuracy gets improved, and there are two layers of interpolation. The first-layer interpolation is to use Lagrange polynomials to approximate the physical variables, and the second-layer interpolation is to eliminate the degree of freedom of the virtual nodes by meshless method. By using the Burton-Miller formulation, the problem of non-uniqueness of the solution is eliminated. Numerical examples for acoustic problems have illustrated that the DiBFM using binary tree grids is superior to conventional BEM, and has the ability to solve practical engineering problems.

To solve large-scale engineering problems of acoustic problems, the fast algorithms such as adaptive cross approximation (ACA) and fast multipole method (FMM) would be introduced in the future work.

Declaration of Competing Interest

The authors declare that they have no known competing financial interests or personal relationships that could have appeared to influence the work reported in this paper.

The authors declare the following financial interests/personal relationships which may be considered as potential competing interests:

JianMing Zhang reports financial support was provided by National Natural Science Foundation of China. Jianming Zhang reports a relationship with Hunan University that includes: employment.

Data availability

No data was used for the research described in the article.

Acknowledgments

This work was supported by National Natural Science Foundation of China under grant numbers 11772125 and 11972010.

References

[1] Cheng AHD, Chen CS, Golberg MA, et al. BEM for theomoelasticity and elasticity with body force-a revisit. Eng Anal Bound Elem 2001;25:377–87 [J].
[2] Shu XM, Zhang JM, H L, Dong YQ. A surface-to-surface scheme for 3D contact problems by boundary face method [J] Eng Anal Bound Elem 2016;70:23–30.
[3] Zieniuk E. Potential problems with polygonal boundaries by a BEM with parametric linear functions [J] Eng Anal Bound Elem 2001;25:185–90.
[4] Peake MJ, Trevelyan J, Coates G. Extended isogeometric boundary element method (XIBEM) for three-dimensional medium-wave acoustic scattering problems [J] Comput Methods Appl Mech Eng 2015;284:762–80.
[5] Copley LG. Fundamental results concerning integral representations in acoustic radiation [J] J Acoust Soc Am 1968;44:28–32.
[6] Schenck HA. Improved integral formulation for acoustic radiation problems [J] J Acoust Soc Am 1968;44:41–58.
[7] Burton AJ, Miller GF. The application of integral equation methods to the numerical solution of some exterior boundary-value problems [J] Proc R Soc Lond 1971;323:201–10.
[8] Guiggiani M, Krishnasamy G, Rudolphi TJ, et al. A general algorithm for the numerical solution of hypersingular boundary integral equations [J] J Appl Mech 1992;59:604–14.
[9] Liu YJ. On the simple-solution method and non-singular nature of the BIE/BEM-a review and some new results [J] Eng Anal Bound Elem 2000;24:789–95.
[10] Gao XW, Feng WZ, et al. A direct method for evaluating arbitrary high-order singular curved boundary integrals [J] WIT Trans Modelling Simul 2013;56:335–51.
[11] Zhang JM, Qin XY, Han X, Li Y. A boundary face method for potential problems in three dimensions [J] Int J Numer Methods Eng 2009;80:320–77.
[12] Zhang JM, Hunag C, et al. Automatic thermal analysis of gravity dams with fast boundary face method [J] Eng Anal Bound Elem 2014;41:111–21.
[13] Zhang JM, Lin WC, Dong YQ, Ju CM. A double-layer interpolation method for implementation of BEM analysis of problems in potential theory [J] Appl Math Model 2017;51:250–69.
[14] Zhang JM, He R, et al. A dual interpolation boundary face method with Hermite-type approximation for elasticity problems [J] Eur J Mech /A Solids 2020;82.
[15] Zhang JM, Ju CM, et al. A binary-tree subdivision method for evaluation of singular integrals in 3-D BEM [J] Eng Anal Bound Elem 2019;103:80–93.
[16] Li G, Aluru NR. Boundary cloud method: a combined scattered point/boundary integral approach for boundary-only analysis [J] Comput Methods Appl Mech Eng 2002;191:2337–70.
[17] Li G, Aluru NR. A boundary cloud method with a cloud-by-cloud polynomial basis [J] Eng Anal Bound Elem 2003;27:57–71.
[18] Lancaster P, Salkauskas K. Surfaces generated by moving least squares methods [J] Math Comput 1981;37(155):141–58.
[19] Zhang JM, Lin WC, et al. A dual interpolation boundary face method for exterior acoustic problems based on the Burton-Miller formulation [J] Eng Anal Bound Elem 2020;113:219–31.
[20] Liu YJ. Fast multipole boundary element method - Theory and applications in engineering. Cambridge University Press; 2009 [M].
[21] Zheng CJ, Chen HB, et al. Is the Burton-Miller formulation really free of fictitious eigenfrequencies? [J] Eng Anal Bound Elem 2015;59:43–51.
[22] Chen X, He Q, Zheng CJ, et al. A parameter study of the Burton–Miller formulation in the bem analysis of acoustic resonances in exterior configurations [J] J Theoret Comput Acoustics 2021;29:2050023.
[23] Zheng CJ. Wideband fmbem for 3D acoustic sensitivity analysis. University of Science and Technology of China; 2011 [D].